Rare Metal Materials and Engineering
Volume
Available online at **www.rmme.ac.cn**

Cite this article as: Rare Metal Materials and Engineering,

DOI: 10.12442/j.issn.1002-185X.20240270

High-Temperature Oxidation and Corrosion and Wear Resistance of Laser Cladding Co-based Coatings on Zr Surface

Xia Chaoqun [1], Yang Bo [1], Liu Shuguang [2], Zhang Bo [3], Zhong Hua [4], Li Qiang [1]

[1] Tianjin Key Laboratory of Materials Laminating Fabrication and Interface Control Technology, School of Materials Science and Engineering, Hebei University of Technology, Tianjin 300130, China; [2] Engineering Research Center for Electrophysical Apparatus and Application Technology, Beijing Research Institute of Automation for Machinery Industry Co., Ltd., Beijing 100120, China; [3] Tianjin Key Laboratory of Molecular Optoelectronic Sciences, Department of Chemistry, School of Sciences, Tianjin University, Tianjin 300072, China; [4] School of Advanced Manufacturing Engineering, Hefei University, Hefei 230000, China.

Abstract: This paper is to prepare Co-based alloy-coated metal Zr using laser melting and cladding technology, to study the difference between the high-temperature oxidation behavior of pure metal Co coatings and Co-T800 alloy coatings, as well as the wear resistance of the coatings, and also to investigate the effect of changing the laser melting process on the coatings. The oxidation weight gain of two coated Zr alloy samples at 800~1200 ℃ and the high-temperature oxidation behavior at high temperature for 1h were studied. The analysis of the results showed that the Co coating and the Co-T800 coating have better resistance to high-temperature oxidation. After oxidizing at 1000 ℃ for 1 h, the thickness of the oxide layer of the uncoated sample was 241 μm, while the thickness of the oxide layer of the Co-based coated sample was only 11.8~35.5 μm. The friction wear test showed that the depth of the abrasion mark of the coated specimen is only 1/2 of the substrate, and the hardness and wear resistance of the Zr substrate have been greatly improved. The disadvantage of Co-based coatings is the reduced performance of corrosion resistance in 3.5% NaCl solution.

Key words: Zr metal, Laser cladding, Co-based coating, High-temperature oxidation resistance, Wear resistance

Zirconium (Zr) and Zr alloys are chemically stable, a high-strength, easily ductile, corrosion-resistant metallic material with the advantage of having a small thermal neutron absorption cross-section that other metals do not have [1-5]. Metal Zr has an indispensable place in many significant capacity areas despite their exceptional benefits, which include good mechanical properties in high-temperature and high-pressure water environments, good corrosion resistance, and the ability to effectively prevent the escape of nuclear fission products [6]. However, Zr also has several disadvantages, including pitting corrosion, low hardness, poor wear resistance, and oxidization at elevated temperatures [7]. It is crucial to boost the stability of Zr metal in use and enhance its resistance to oxidation, corrosion, and surface wear in order to prolong the metal's useful life and address this issue.

Many surface modification techniques have emerged in recent years, including laser cladding [8], magnetron sputtering [9-12], hot and cold spraying [13], micro-arc oxidation [14,15], and ion implantation [16]. Nowadays, a common research avenue to increase material qualities is reinforcing material surfaces to enhance their properties. Surface modification can be used to target a material's surface according to desired qualities and

Received date:
Foundation item: National Natural Science Foundation of China (Grant no. 52071126)
Corresponding author: Xia Chaoqun, Ph.D., Professor, Tianjin Key Laboratory of Materials Laminating Fabrication and Interface Control Technology, School of Materials Science and Engineering, Hebei University of Technology, Tianjin 300130, P. R. China, E-mail: chaoqunxia@hebut.edu.cn

provide a notable improvement in a specific area's performance. Its benefits include a short research and development cycle, rapid results, little raw material usage, energy savings, reduced emissions, adaptability to various environments with different coatings, and more [17].

The laser cladding technique creates a protective layer by rapidly melting the cladding material and the material surface under laser irradiation and cooling the molten pool [18]. The coating is typically in a strong metallurgical bond with the base metal because of the special mechanism of laser cladding; as a result, the surface of the material experiences a variety of surface property changes depending on the type of coating material used [19]. The laser cladding technique offers several advantages [20,21], including the ability to easily achieve a fine grain organization, high hardness, a small heat-affected region, compatibility with a wide range of materials, high material utilization rate, and absence of chemical contamination, among others. In their study, Kim et al. [22] employed the laser cladding approach to fabricate a uniform chromium coating on the surface of a zinc alloy. The oxidized weight gain of the Cr-coated samples was only 1/29 of that of the uncoated samples. Furthermore, after undergoing oxidation for 2000 s at a high temperature of 1200 ℃, the oxidized thickness of the Cr coatings was significantly lower than that of the base samples, indicating a high potential for development.

Co-based alloys and their composites exhibit favorable characteristics such as excellent high-temperature performance, notable resistance to corrosion and wear, and a diverse array of uses in high-temperature settings [23]. In a general sense, cobalt alloys exhibit two distinct crystal structures: face-centered cubic and densely organized hexagonal. The clustered hexagonal structure is characterized by higher hardness and comparatively lower ductility [24]. The incorporation of cobalt (Co), chromium (Cr), tungsten (W), and other elements into the powder has the potential to enhance the wear resistance of the coating and enhance its performance under high-temperature conditions. The incorporation of silicon (Si) element facilitates the process of grain refinement, while concurrently promoting the deoxidation of slag. Currently, there is limited literature on cobalt-based alloys with Zr alloys. However, there is a growing interest in using cobalt-based alloy coatings to modify the surface of Ti alloys. Scientists applied a Co coating onto the titanium alloy surface and observed that the coating primarily consisted of columnar crystals, with a minor presence of dendritic crystals and other structures. Additionally, the coating's hardness is approximately three times greater than that of the substrate [25].

The utilization of cobalt-based materials exhibits significant promise in the realm of laser cladding materials. In their study, Shahroozi et al. [26] showed that including modest quantities of Ti and C elements in Co-based powders can enhance the coating's hardness. The rationale behind this phenomenon is in the ability of these two elements to undergo reactions with Co, resulting in the formation of compounds. The presence of these compounds facilitates nucleation, thereby contributing to the process of grain refinement and enhancing the wear resistance of the coating. In their investigations, Weng Fei et al. [27,28] found that incorporating TiN, B_4C, and SiC hard particles into cobalt-based alloys can enhance the hardness and wear resistance of the coatings. The study additionally showed a strong correlation between the organization of the coating and the shape of the melt pool. Consequently, it is evident that both the formation and duration of the melt pool play a crucial role in achieving optimal coating organization.

The main innovation of this experiment is the use of laser cladding technology to prepare Co-based alloy coatings on the surface of metallic zirconium, which is less researched in the surface treatment of metallic zirconium, and this paper systematically analyzes the influence of Co-based coatings on the surface properties of metallic Zr from various perspectives, such as high temperature oxidation, corrosion resistance, hardness ,and wear resistance. It provides a theoretical basis for the new surface treatment method of metal Zr.

1 Experiment

1.1 Sample preparation

The present study utilized pure Zr plates as the experimental material. Before experimenting, the Zr plates underwent a wire-cutting process to transform them into metal plates with dimensions of 100 mm×200 mm, which were deemed adequate for laser cladding. To eliminate oxides from the metal surface, the cut sheet is subjected to sanding using sandpaper with a grit of 60#. Additionally, alcohol cotton is employed to eliminate any surface oil.

Fig.1 displays the SEM images of cladding powder. The cladding powders consisted of 99.99% pure spherical Co metal powder and Co-T800 alloy powder, respectively. The chemical composition of Co-T800 alloy is shown in Table 1.

Table 1 The chemical composition of Co-T800 alloy (*wt.*%)

Co	Cr	Ni	Fe	Si	Mo	C	S	S
Bal	17.5	1.41	0.22	3.14	28.1	0.01	0.01	0.01

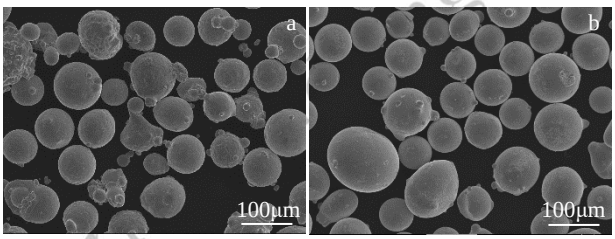

Fig.1 SEM images of powder (a) Co powder (b) Co-T800 powder

The utilization of the YLS-4000-KC CO_2 fiber laser model is implemented through the synchronized delivery of powder. At the operation table, a prefabricated metal Zr plate is positioned,

and the experiment is conducted by employing argon gas synchronized delivery surrounding the laser head to safeguard the material. Before and following usage, it is necessary to vacuum seal and preserve the powder. Before laser melting, the powder material must undergo sieving using a 100 mesh sieve to separate the larger particles to maintain the smoothness of the powder during the melting process. The sifted powder is then dried in a vacuum drying oven at a temperature of 200 ℃. Once dried, it is sealed and stored.

The preparation of Co-coated and Co-T800-coated Zr metal was conducted using certain process parameters. These parameters included a laser power of 1800 W, a scanning speed of 50 mm/s, a powder feed rate of 1.2 L/min, and a lap rate of 50%. The process parameters of Co-T800 alloy coating were modified to a scanning speed of 30 mm/s while keeping all other parameters constant. The coatings before and after the process adjustment were labeled as $T800_1$ and $T800_2$, respectively. The Co metal coating process parameters were set to a laser power of 2000 W while keeping all other parameters constant. The coatings before and after the process modification were labeled as Co_1 and Co_2, respectively. Table 2 presented below illustrates the correlation between the laser melting coating and the various process parameters.

Table 2. Laser cladding coatings and process parameters

Coating	Laser power	Scanning speed	Powder feeding capacity
$T800_1$	1800 W	50 mm/s	1.2 L/min
$T800_2$	1800 W	30 mm/s	1.2 L/min
Co_1	1800 W	50 mm/s	1.2 L/min
Co_2	2000 W	50 mm/s	1.2 L/min

The laser-coated samples were first chopped using an EDM wire cutter into cubes measuring 10 × 10 × 10 mm^3. The coatings were then smoothed on the surface using sandpaper. The samples were then cleaned using an ultrasonic cleaner in alcohol for ten minutes to get rid of all surface contaminants. To make sure the surfaces were totally dry, the samples were lastly cleaned and dried. There were five sets of parallel trials set up: $T800_1$, $T800_2$, Co_1, Co_2 coating, and Uncoated.

1.2 Experiments and Methods

The microscopic morphology was seen at high magnification using a scanning electron microscope (SEM, JSM-7100). The metallographic examination involved examining the metallographic organization of the coated surface and cross-section following corrosion. The X-ray diffractometer (XRD, Bruker D8) was employed to examine the surface composition of the coatings. The scanning speed was set at 6 degrees per minute, and the scanning range spanned from 10 to 90 degrees. Analyzed utilizing MDI Jade analytical software, the peak XRD curves were examined. The analysis of the elements distribution of the coated cross section was conducted utilizing an Energy Dispersive Spectrometer (EDS).

A high-precision electronic balance (FA1204B) was used to measure the starting weight of the coated sample. A muffle furnace (KSL-1200X) was used to investigate the high-temperature oxidation behavior of coated Zr metal samples compared to uncoated Zr metal controls in an air atmosphere. The experimental group was subjected to temperatures of 800 ℃, 900 ℃, 1000 ℃, 1100 ℃, and 1200 ℃ for a duration of 1 h to examine the alterations in coating surface morphology, diffusion layer thickness, and other related factors about temperature. The protocol for high-temperature oxidation was established in the following manner: The temperature was initially set at 20 ℃, with a ramp rate of 5 $℃·min^{-1}$. The temperature was then maintained at a steady rate as it gradually increased to the goal temperature for a duration of one hour. Subsequently, the temperature was cooled to room temperature using a furnace. To ensure precise quantification of the mass alteration of the specimens before and after high-temperature oxidation, all samples subjected to high-temperature oxidation were positioned within a ceramic crucible. Following the oxidation process, the weight of the oxidized coating samples was once again documented utilizing an electronic balance. To determine the oxidized weight gain per unit area of the coating, the mass change and surface area of the sample were taken into account.

The corrosion resistance of the coatings was assessed using an electrochemical workstation (CHI660E). The corrosion process involves the utilization of a 3.5% NaCl solution with a mass fraction of 3.5% NaCl. This solution is composed of high-purity NaCl and deionized water. By employing this NaCl solution, the corrosion characteristics of Zr metal in high-salt environments can be replicated, thereby simulating the marine environment. The sample had a contact area of 0.5 cm^2. A fixture is used to securely attach the surface of the sample to the electrochemical workstation, ensuring direct contact with the corrosive solution. The initial measurement of the open-circuit potential (E_{ocp}) of the sample under investigation was conducted, followed by the maintenance of a stable open-circuit potential for a duration of 1800 seconds. The initial potential of the electrochemical impedance was determined by inputting the measured value of the stabilized open-circuit potential. Subsequently, the electrochemical impedance spectra (EIS) of the samples were obtained, and impedance measurements were conducted within the frequency range of 10^{-2} to 10^{-5} Hz, with an amplitude of 0.01 V. The data that was acquired was subjected to curve fitting using the ZSimpWin impedance program to derive the fitted equivalent circuit and parameters. The electrochemical polarization curves were established with measurement conditions including a scanning speed of 0.01 V s^{-1} and a scanning range spanning from -1.0 V to 2.5 V. The electrochemical polarization curves were acquired to determine the corrosion potential (E_{corr}) and breakdown potential (E_b).

The Vickers hardness of the substrate and the surface of the

coated samples after laser cladding were characterized using a microhardness tester (HMV-G-XY-S). A positive quadrangular conical diamond indenter was utilized as the indenter in the hardness tester. The Vickers hardness was determined by measuring the diagonal length of the indentation and subsequently calculating the associated Vickers hardness. Eight distinct places were randomly chosen to focus and spot in each sample plane. The applied stress load was 0.2 kgf, with a symbol gauge of $HV_{0.2}$. The load retention duration was set at 10 seconds.

The Comprehensive Material Surface Properties Tester (CFT-I) was used to conduct reciprocal wear tests on the surfaces of the coating and the substrate. These tests had a length of 5 mm. The computer recorded the changes in the coefficient of friction during the friction process. A profilometer was used to measure the profile of the abrasion marks after friction. The friction partner was chosen based on the friction of ceramic balls with a diameter of 5 mm. The test was conducted for 15 minutes with an applied load force of 20 N and a friction speed of 200 cycles per minute.

When conducting experiments, the primary consideration is to ensure the safety of the experiment, followed by the reproducibility of the experiment.

2 Results and Discussion

2.1 Microstructure and Physical Phase

The post-laser cladding surface of the coating will exhibit undulating streaks resulting from the superimposed laser movement on the substrate's surface. Consequently, it is necessary to subject the coating surface to processing and sanding using sandpaper. Fig.2 displays the macroscopic structure of the $T800_1$, $T800_2$, Co_1, and Co_2 coated samples, respectively. Additionally, it shows the detailed sections. The figure illustrates that the coatings exhibit a relatively smooth and flat surface, devoid of apparent defects, and possess a high level of density. Upon magnification at a 50-fold level, it becomes evident that the four coatings exhibit the presence of minuscule air holes, as indicated by the arrows in the figure. Additionally, there are also minuscule cracks that are not readily detectable. The Co-T800 alloy coating surface has a similar macroscopic shape to the Co coating, and its overall performance is more compact and consistent, making it suitable for achieving a high-performance coating. Fig.3 depicts the micro-morphological arrangement of the surfaces of Co coating samples as observed through a scanning electron microscope at a magnification of 5000 times. The surface microstructure of the four sample groups exhibits the presence of dendrites and cytocrysts, which are observed to be intermixed with one another. This organization was established as a result of the accelerated cooling of the laser fusion coating, which promotes dendritic growth. This hybrid organization exhibits exceptional mechanical capabilities. The development of this tissue is primarily influenced by the pace of cooling, with no substantial association observed with the energy density of the laser.

The optimization of process parameters is of utmost importance in the context of laser cladding. To modify the energy density of the laser, it is necessary to decrease the scanning speed and augment the laser power. The objective of these modifications is to attain coatings that exhibit superior quality and
performance while maintaining the structural integrity of the substrate. Hence, it is imperative to exercise meticulous control
and optimization over these process parameters to achieve the intended coating outcome. The impact of process parameters on laser cladding coatings is highly intricate. For a comprehensive

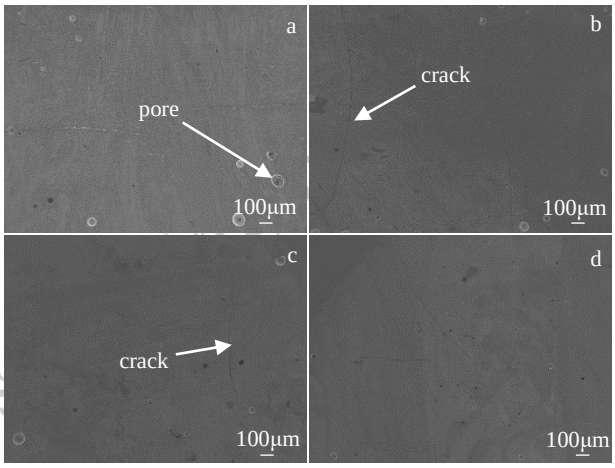

Fig.2 SEM images of coating (a) $T800_1$ (b) $T800_2$ (c) Co_1 (d) Co_2 coating

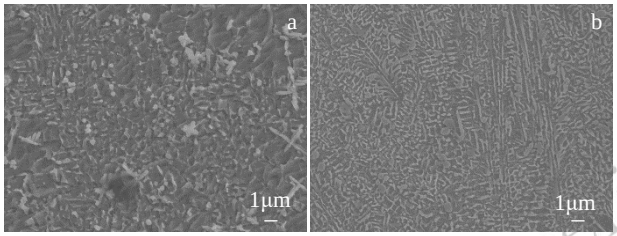

Fig.3 SEM images of Co coating at a magnification of 5000 times (a) Co_1 (b) Co_2 coating

examination of the influence of process parameters on coating properties, it is necessary to conduct numerous repetitive experiments to analyze the underlying principles. However, this chapter primarily focuses on the performance evaluation of Co-based coatings, resulting in a relatively limited investigation into the effects of increasing laser energy density on coating performance.

Fig.4 displays the X-ray diffraction (XRD) study findings regarding the surface of laser-melted Co-T800 coating and Co coating. The XRD curves exclusively exhibit the diffraction peak associated with Co on both coating surfaces. The Co coating exhibited a higher peak, which aligned with the stand-

ard diffraction card of Co metal. Conversely, the XRD analysis of the Co-T800 alloy coating revealed a slight displacement in the position of the diffraction peak, but it remained similar to the Co diffraction peak. However, the intensity of the diffraction peak was lower. XRD analysis operates on the fundamental premise of exposing certain crystalline surfaces within a metal to parallel X-rays. These irradiated X-rays cause interference between the mutually parallel crystalline surfaces, resulting in the appearance of diffraction peaks on the XRD pattern. Hence, the primary factor contributing to the diminished peak value observed in the Co-T800 coating can be attributed to the alloy coating containing additional metal elements. These metal atoms are solidly dissolved within the Co lattice gap, leading to crystal structure distortion in the Co lattice. Consequently, the interference effect of X-rays on the crystal face is diminished, resulting in the manifestation of weak diffraction peaks in the XRD pattern.

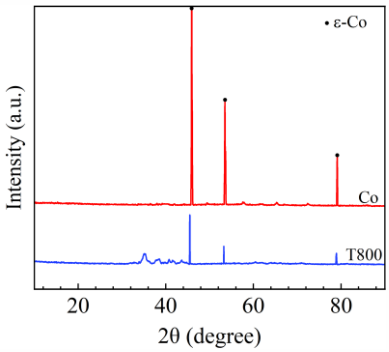

Fig.4 XRD pattern of Co and Co-T800 laser cladding coating

Scanning electron microscopy and energy spectroscopy can provide a clear determination of the elemental distribution of the coating cross-section and diffusion layer. The thickness of the coating was determined by scanning the cross-section of the coating, as depicted in Fig.5. The laser cladding $T800_1$ coating had a thickness of 331.9 μm, the $T800_2$ coating had a thickness of 613.1 μm, the Co_1 coating had a thickness of 547.5 μm, and the Co_2 coating had a thickness of 635.6 μm. Through the manipulation of laser process parameters, it was observed that the thickness of both laser melting coatings, namely Co-T800 and Co, exhibited an upward trend as the laser energy density rose. Furthermore, the morphology of the coating cross-section is observable, revealing a consistent transition between the coating and the substrate in all four samples. The interface between the coating and the substrate is readily apparent, devoid of any apparent defects.

The cross-section micro-scans of the Co-T800 coating and Co coating before and after the enhancement of the coating process parameters, along with the EDS results, are depicted in Fig.6(a-b). These images provide a clear representation of the elements present in the cross-section of the coated samples. Fig.6(a) displays the $T800_1$ coating, revealing that the upper half of the coating primarily consists of Co, Mo, and Cr elements, with a little presence of evenly distributed Si elements. Additionally, the distribution of Zr elements is also observed. The predominant elemental composition in the lower portion of the substrate is primarily Zr. In the coating, the concentration of Zr is comparatively lower than that found in the substrate.

During the laser cladding process, the inclusion of a tiny quantity of Si elements can effectively adsorb contaminants and enhance the purity of the molten pool on the substrate's surface.

Additionally, the incorporation of Mo and Cr elements can contribute to the reinforcement of the coating. The coating exhibits a more homogeneous distribution of elements, devoid of elemental bias aggregation, so establishing a solid basis for generating a coating with favorable performance characteristics.

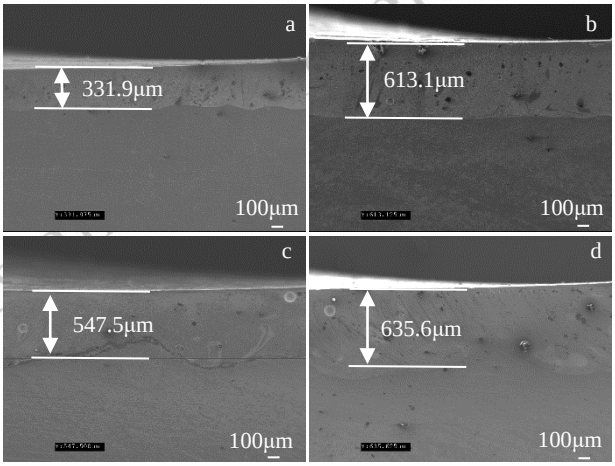

Fig.5 SEM images of thickness of laser fusion coating: (a) $T800_1$ (b) $T800_2$ (c) Co_1 (d)Co_2 coating

The performance of the coating is contingent upon the compatibility and bonding process between the coating and the substrate. The establishment of robust compatibility between the coating and the substrate is crucial to prevent the occurrence of flaking and peeling, hence enhancing the longevity and stability of the coating's performance.

In contrast to Co-T800 coatings, pure metal Co coatings lack additional metal components, resulting in the absence of lattice distortions. Consequently, these coatings exhibit enhanced flexibility and improved resistance to high-temperature thermal shocks. However, it is important to note that the strength of pure metal Co coatings is comparatively lower. The cross-sectional micrographs of the metal Co coating before and after the enhancement of the coating process parameters, along with the EDS results, are depicted in Fig.6 (c-d). These micrographs reveal the presence of Co and Zr elements in the coating. Additionally, the XRD analysis of the coating reveals that Co is the predominant phase, while Zr is firmly dissolved within the lattice interstitials within the

solid solution of Co. Co_2 coatings exhibit a comparable elemental distribution to Co_1 coatings, except for variations in thickness.

2.2 High-temperature oxidation properties

High-temperature oxidation experiments were conducted on the samples from the experimental group and the control group specimens at temperatures of 800 ℃, 900 ℃, 1000 ℃, 1100 ℃, and 1200 ℃, respectively. According to Fig.7, the surface morphology of the substrate surface and various coating surfaces were examined using a microscope and scanning electron microscope following oxidation at a high temperature of 1000 ℃ for a duration of 1 hour. Following oxidation at elevated temperatures, the uncoated sample exhibited a white hue on its surface, accompanied by prominent irregular cracks and heightened peeling. These observations suggest that the substrate's surface had undergone significant oxidation. Conversely, the Co-based coating samples produced using the laser cladding approach exhibited little surface fissures upon oxidation.

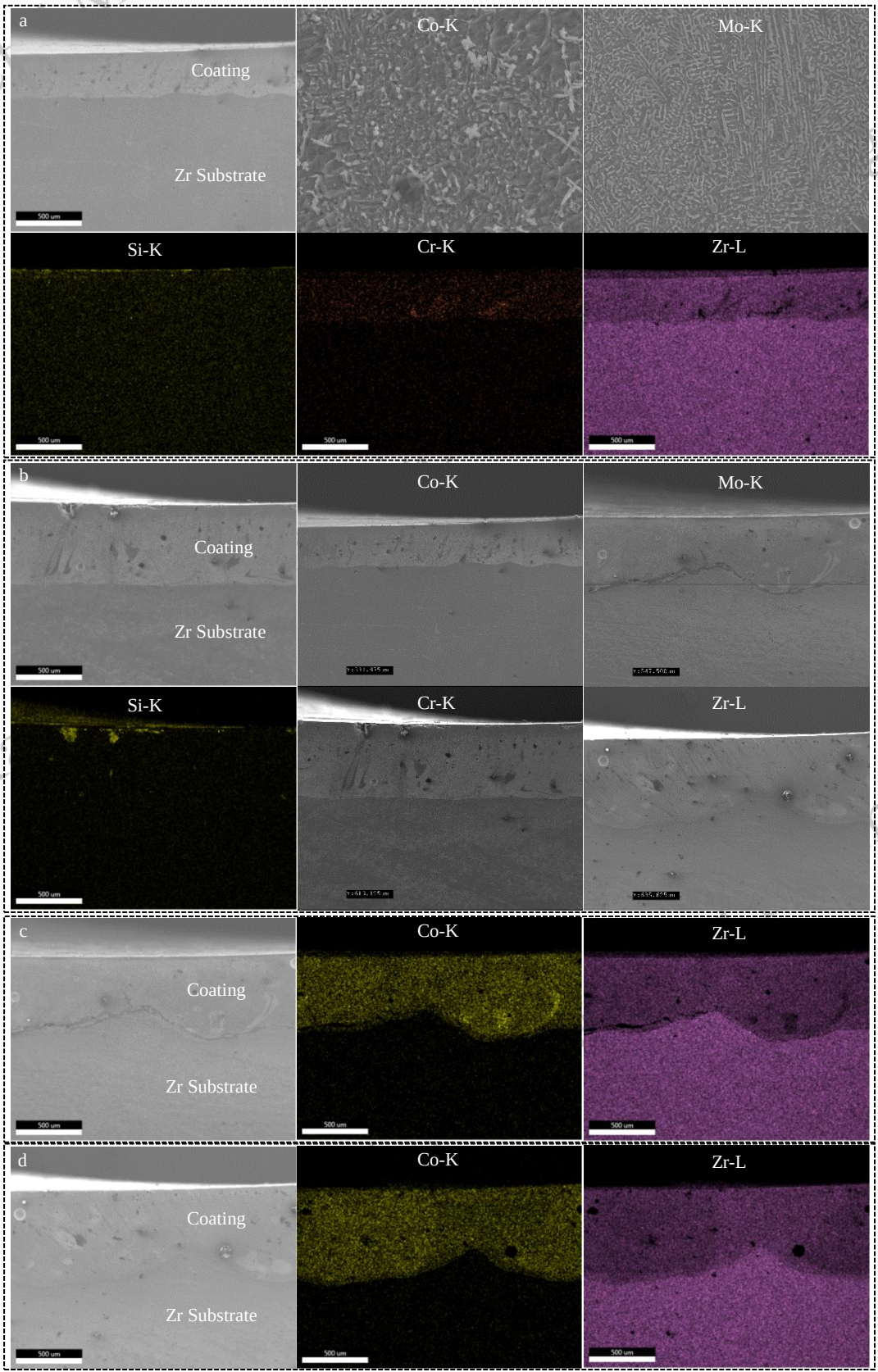

Fig.6 Scan of microscopic cross-section of laser melted Co-T800 coating and Co coating and EDS results: (a) $T800_1$ coating (b) $T800_2$ coating (c) Co_1 coating (d) Co_2 coating

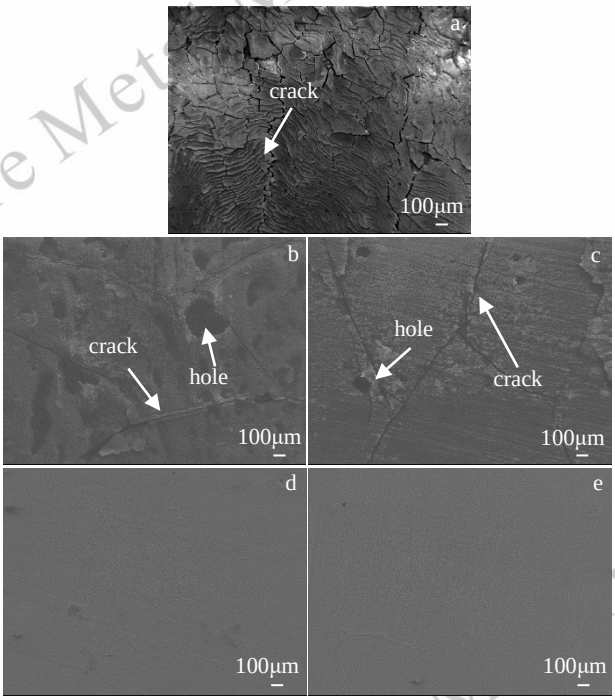

Fig.7 SEM image of different sample surfaces after oxidation at 1000 ℃ for 1 hour: (a) Uncoated (b) $T800_1$ (c) $T800_2$ (d) Co_1 (e) Co_2 coating

The presence of cracks on the surface of the Co-T800 coating is evident, albeit with a significantly lower quantity and density compared to the substrate sample. Upon magnification at 1000 times, the surface morphology of the coating demonstrates a consistent homogeneity and density, with only a minor number of cracks. In contrast to the Co-T800 alloy coating, the Co-metal coating exhibits superior performance after oxidation at a temperature of 1000 ℃. The coating exhibits a high level of density, with no visible cracks or faults upon magnification. This suggests that the coating effectively safeguards the substrate and significantly extends its lifespan at elevated temperatures.

The quantity of oxygen assimilated by the surface of the sample can be observed by measuring the alteration in weight of the sample before and following oxidation. Fig.8 displays the outcomes of oxidized weight gain, indicating that the weight of all samples in the experimental group exhibited an upward trend as the oxidation temperature increased. However, it is noteworthy that the disparity in oxidized weight gain between the coated and uncoated specimens became increasingly prominent as the temperature escalated. Significantly decreased oxidized weight growth is observed in the specimens of the coated group compared to the control group, particularly at temperatures of 1100 ℃ and 1200 ℃. The visual representation of the coating's oxidation resistance can be enhanced by quantifying the extent of oxygen absorption on the surface of the sample.

The examination of the outcomes of oxidation weight gain indicates that the specimens coated with Co demonstrate superior resistance to oxidation at high temperatures compared to the substrate. Fig.9 presented below illustrates the measuring of the oxide layer thickness obtained from the scanning of the uncoated sample, the Co-T800-coated sample, and the two Co-coated specimens, along with the corresponding EDS results. The sample's surface was examined using a scanning electron microscope to measure the oxide layer. The results indicate that the uncoated substrate specimen has more pronounced oxidation, and the interfaces of the oxide layer display a crisp laminar structure.

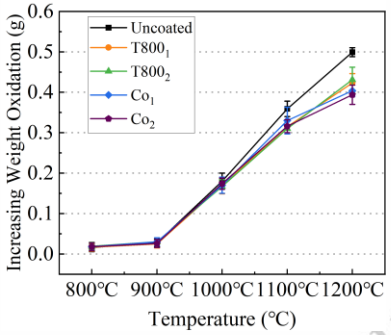

Fig.8 Oxidized weight gain of different coated samples oxidized at 800 ℃-1200 ℃ for 1h

Elemental oxygen diffuses into the substrate, including the oxide layer, to a distance of nearly 240 μm. The $T800_1$ coating exhibited a surface oxidation thickness of approximately 11.8 μm. Similarly, the $T800_2$ coating displayed a comparable oxidation thickness of approximately 11.8 μm. The Co_1 coating displayed a thickness of approximately 20.9 μm, while the Co_2 coating exhibited a thickness of approximately 35.5 μm. The oxidation thickness of the samples in the coating group is significantly surface. This suggests that, at elevated temperatures, the Co-based coating specimens exhibit a slower rate of oxida-

tion compared to the Zr substrate. Additionally, the coated samples demonstrate superior anti-oxidant properties. The EDS analysis reveals that the oxygen element is predominantly localized within the oxide layer, where oxidation predominantly takes place on the coating's surface.

However, upon examining the oxygen element distribution depicted in Fig.9 (b-c), it becomes evident that elevated levels of oxygen are also present within the cracks of the coatings. This observation implies that the oxygen element has the potential to facilitate deeper oxidation towards the substrate through these cracks. In contrast to the Co-T800 coating, the metal Co coating exhibits a lack of cracks during oxidation, thus preserving the integrity of the coating. However, it is worth noting that the Co coating experiences a greater degree of oxidation, resulting in a greater thickness compared to the Co-T800 coating. Therefore, it can be inferred that the pure metal coating exhibits superior thermal stability compared to the alloy coating. Additionally, the coating demonstrates good molding quality. On the other hand, the alloy coating exhibits higher resistance to oxidation than the

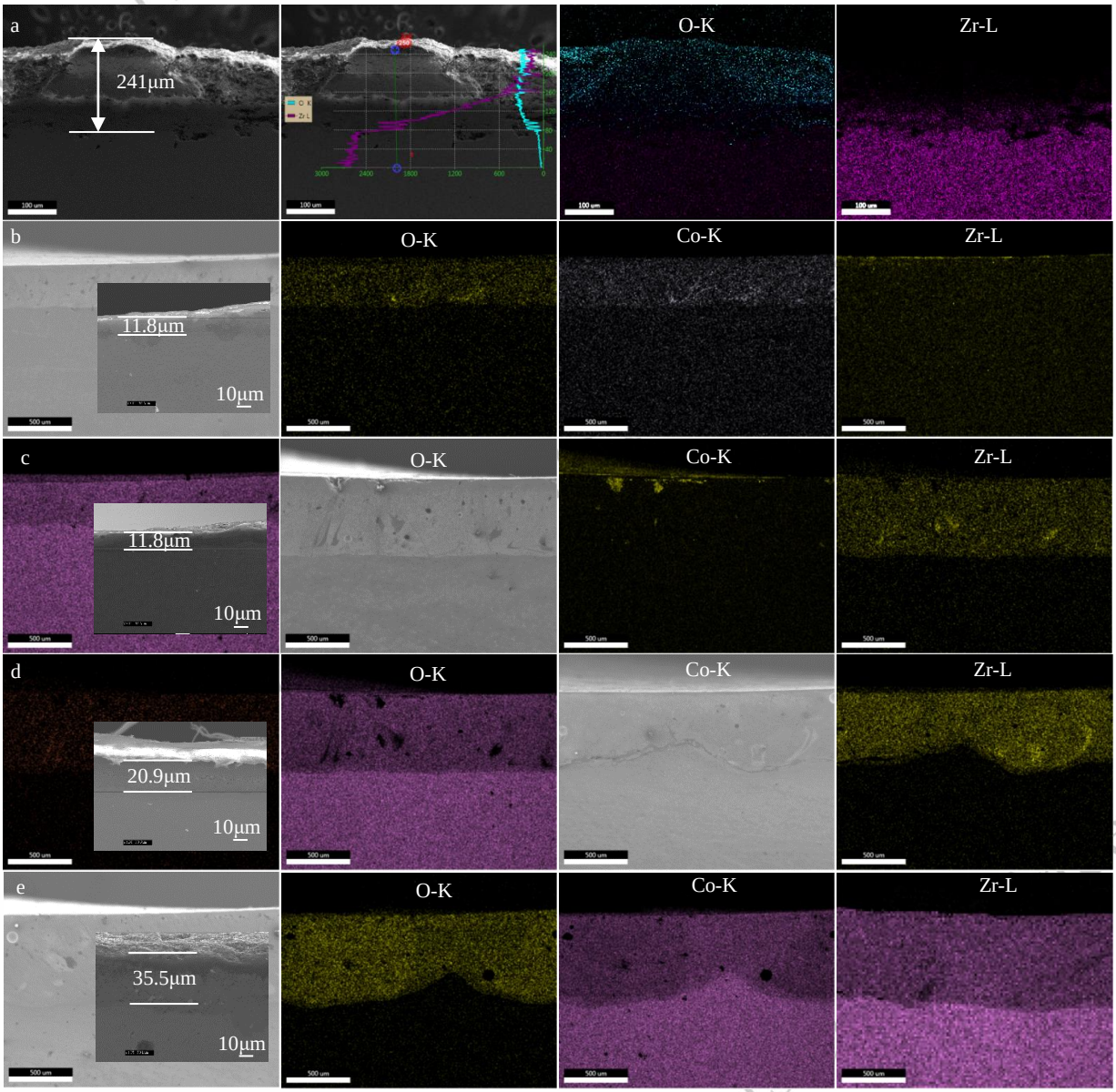

Fig.9 Oxide layer thicknesses measured under scanning electron microscope for different samples and corresponding EDS results: (a) Uncoated (b) $T800_1$ (c) $T800_2$ (d) Co_1 (e) Co_2 coating

pure metal coating. However, it has an inferior heat resistance and is prone to cracking and defects.

The disparity in high-temperature oxidation between the coating and the substrate becomes increasingly evident as the oxidation temperature rises. After a high temperature at 1200℃ oxidate for 1 h, the Co-T800 coating exhibits notable surface

deterioration, characterized by extensive cracking and peeling of

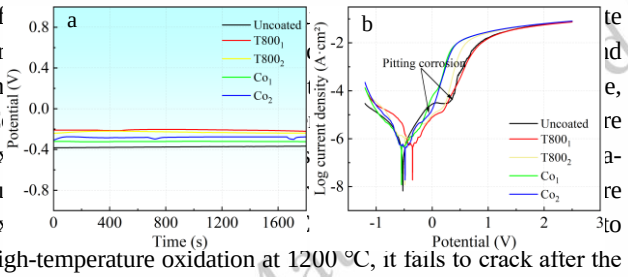

high-temperature oxidation at 1200 °C, it fails to crack after the coating. Despite having a slightly thicker oxide layer than the alloy coating, the Co coating effectively prevents the further diffusion of oxygen atoms after high-temperature oxidation at 1200 °C. Therefore, it serves to safeguard the substrate specimen and enhance the resistance of the substrate surface to oxidation at elevated temperatures.

It is found that the surface of the uncoated substrate has serious cracking after high temperature oxidation, while the surface of the Co coating remains intact after high temperature. This is because ZrO_2 at 800-900 °C has a transition from the tetragonal crystal structure phase to monoclinic crystal structure, the volume will occur 3-5% expansion, resulting in cracking. The thermal stability of CoO is better, and there is no structural transformation, so the coating surface remains intact.

2.3 Electrochemical corrosion property

In Fig.10 (a), the open-circuit potential versus time curves for the laser melting specimen and the substrate specimen in a 3.5% NaCl solution are depicted. The experimental findings indicate that the open-circuit potentials of the Co coating and the Co-T800 coating surpass those of the substrate specimen. The polarization curves of the uncoated substrate and the coated sample in a 3.5% NaCl solution are depicted in Fig.10 (b). The corrosion potential (E_{corr}) in the polarization curve depicted in the figure represents the pivotal moment when the curve transitions from a downward trend to an upward one, as well as the point of minimum value on the curve. The corrosion potential is indicative of the sample's potential at the onset of corrosion, with higher values indicating greater difficulty in initiating the corrosion reaction. The breakdown potential, denoted as Eb, refers to the electronic breakdown of the sample surface passivation film. When the potential value is altered, the polarization curve undergoes a transition from a smooth to a sudden increase. The arrow in the figure indicates the position where the breakdown potential occurs. This shift signifies the stability of the passivation film's reaction and the strength or weakness of its breakdown potential. A higher potential value indicates greater stability of the passivation film, resulting in improved corrosion resistance.

Fig.10 (a) Open circuit potential (b) polarization curve

The polarization curves demonstrate that the corrosion potentials of the Co-based coatings exhibit higher values in comparison to the substrate. This observation suggests that the coatings exhibit greater corrosion resistance when compared to the Zr substrate. Furthermore, the corrosion potentials align with the findings obtained from the open circuit potentials. Nevertheless, the Co-based coatings exhibited reduced breakdown potentials compared to the Zr-based specimens, suggesting that the passivation film on the coatings' surface had diminished corrosion resistance. The observed phenomenon of higher corrosion potential and lower breakdown potential in the presence of a curve is still prevalent. This can be attributed to the presence of small cracks on the laser-melting coating surface, which significantly impacts the stability of the passivation film. Consequently, the equilibrium state of the passivation film is disrupted, leading to the corrosion of the sample under examination from a kinetics perspective. From a kinetic perspective, the initiation of corrosion will lead to an escalation in the corrosion rate of the specimen under examination. The electrochemical polarization curve characteristics for various samples in a 3.5% NaCl solution are presented in Table 3. The examination of the electrochemical polarization curves reveals that Co-based coatings exhibit lower corrosion resistance compared to Zr substrates. However, Co-T800 alloy coatings demonstrate slightly higher corrosion resistance than pure metal Co coatings. Furthermore, enhancing the laser melting and cladding process parameters has a minimal effect on the corrosion resistance of Co coatings.

Table 3. Parameters of electrochemical polarization curves

Parameters	Uncoated	T800$_1$	T800$_2$	Co$_1$	Co$_2$
E_{corr}(V)	-0.51	-0.37	-0.49	-0.46	-0.53
E_b(V)	0.34	0.25	0.26	-0.01	-0.17

The electrochemical impedance curves (EIS) of various samples in a 3.5% NaCl solution are depicted in Fig.11 (a-c) The

software-fitted equivalent circuits are utilized to analyze the data. The observed high and low impedance values provide evidence of the alloy's exceptional resistance to corrosion. The Nyquist diagram, depicted in Fig.11 (a), displays the real and imaginary components of the impedance, represented by the horizontal and vertical coordinates of the diagram, respectively. The Nyquist diagram serves the purpose of visually representing variations in corrosion resistance based on the curves of distinct samples. The data of these samples is depicted as arcs with varying diameters within the diagram. The diameters of these arcs correspond to the magnitude of charge transfer capacity between the test sample and the electrolyte solution, commonly referred to as capacitive arcs [29]. The capacitance arc, also known as the diameter of the arc, signifies the magnitude of the charge transfer capacity between the test sample and the electrolyte solution. The resistance to charge transfer between the sample and the electrolyte solution increases proportionally with the diameter of the capacitance arc, hence enhancing the corrosion resistance of the sample.

Both the Co-T800 coating and Co coating in the figure have smaller capacitive arc widths compared to the Zr substrate. This suggests that the corrosion resistance of Co-T800 coating and Co coating is weaker than that of the Zr substrate. In Fig.11 (b), the Bode mode diagram illustrates the relationship between the impedance of the mode value and the frequency of the wave. The resistance of the passivation film is represented by the intersection of the sample data line in the figure and the vertical coordinate axis [30]. During the low-frequency stage, the curve exhibits a slope of approximately -1, indicating a straight line. At this point, the resistance primarily arises from the capacitance response. However, when the curve intersects the longitudinal coordinate axis, the passivation film resistance can be approximated. As the frequency increases, the curve exhibits a progressive shift towards a more gradual pattern. During this period, the resistance of the passivation film decreases, suggesting that the resistance at this stage is mostly influenced by the response of the electrolyte resistance.

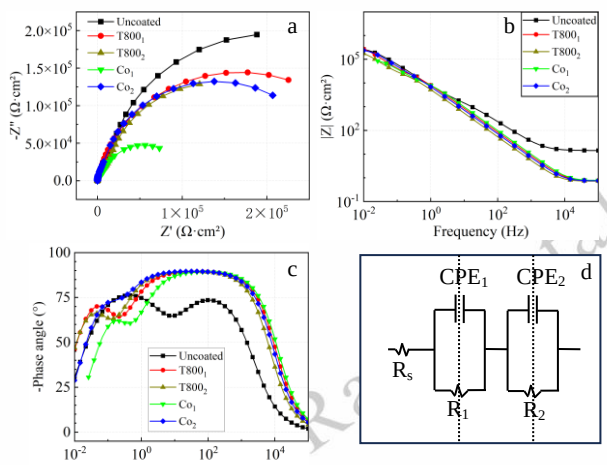

Fig.11 EIS curve: (a) Nyquist diagram (b) Bode mode diagram (c) Bode phase angle diagram (d) Equivalent circuit diagram

The Bode phase angle diagram, as depicted in Fig.11(c), illustrates the relationship between the impedance of the phase angle and the frequency of the electric wave. A greater phase angle peak corresponds to a wider range of peaks, suggesting a higher level of corrosion resistance in the material [31]. The Bode phase diagram, Bode mode diagram, and Nyquist diagram yielded consistent findings, indicating that the samples exhibited corrosion resistance in a 3.5% NaCl solution. The corrosion resistance of the samples followed a general order of Zr > Co-T800 coating > Co coating. The impedance measurements exhibited concurrence with the electrochemical polarization curves. Upon analysis, the primary cause for the disparity in performance can be attributed to two factors: one of which may be attributed to the laser melting procedure, which generates minor fissures on the coating's surface, thereby impairing the corrosion resistance of the Ni-based coating. The second reason could be attributed to the comparatively weaker corrosion resistance of Co in comparison to Zr alloys. Consequently, the application of laser melting techniques to Co coatings on Zr alloys does not effectively enhance the corrosion resistance of the substrate surface. Furthermore, the enhancement of the process parameters did not yield a substantial alteration in the corrosion resistance of the coating, as seen by the comparison. In conjunction with prior experiments, this study demonstrates that the laser cladding process parameters solely influence the molding characteristics of the coating, such as coating thickness and dilution rate. Conversely, the chemical properties of the coating have an indirect impact on the coating's performance, primarily by influencing its macroscopic quality.

Table 4 displays the impedance parameters of the sample. The equivalent circuit diagram model, as depicted in Fig.11(d), was fitted using the ZSimpWin software. This model demonstrates a strong correspondence with the experimental data [32]. In this model, R_s denotes the resistance of the electrolyte solution, R_1 represents the resistance of the passivation film, and R_2

represents the coating resistance. R1 and R2 are connected in parallel with capacitors with capacities respectively. The two parallel circuits are then connected in series with Rs to create the overall fitted circuit. The initial parallel circuit depicts the phenomenon of ion diffusion over the passivation film after traversing parallel circuit illustrates the process of substrate corrosion. The capacitance of the diffusion layer of the passivation film and the protective layer of the coating are denoted as CPE_1 and CPE_2, respectively. These capacities are quantified using the symbols Q_1 and Q_2 [33]. With n representing the dispersion index of the constant phase angle element. This value is associated with the surface roughness of the sample under examination. When the value of n is 0, the capacitance of the CPE can be considered equivalent to the resistance. Similarly, when n is 1, the capacitance can be considered equivalent to the CPE [34].

2.4 Hardness and wear resistance

The evaluation of materials in applications that include dynamic friction and wear, such as bearings, gears, and brushes in mechanical contact, is significantly influenced by hardness and wear resistance. The response of materials to wear is a complex phenomenon that depends on both the wear system and the wear process itself [35]. It is crucial to carefully consider specific material tribology indications while doing linear reciprocating wear tests using controlled environment friction and a wear tester. The reliability of the tested material is contingent upon several critical aspects, namely volume loss, coefficient of friction, and surface abrasion pattern. Researchers can obtain significant insights into the wear properties of different materials under controlled testing conditions by closely monitoring these indicators [36].

Table 4 Impedance parameters of different samples

Samples	R_s(Ω cm^2)	R_1(Ω cm^2)	CPE_1		R_2(Ω cm^2)	CPE_2	
			$Y_{0,1}$(s^{n}Ω^{-1} cm^2)	n		$Y_{0,1}$(s^{n}Ω^{-1} cm^2)	n
Zr	7.08	8.31E2	2.79E-6	0.89	3.34E5	2.45E-5	0.91
$T800_1$	7.71	1.32E4	3.25E-5	0.96	3.91E5	4.52E-5	0.92
$T800_2$	7.24	2.61E5	7.32E-5	0.89	1.35E4	5.06E-5	0.87
Co_1	7.73	9.41E7	4.24E-5	0.90	7.29E3	2.62E-5	0.96
Co_2	7.49	8.06E3	6.39E-6	0.95	2.64E5	3.45E-5	0.87

Hardness tests were conducted on three samples: the Co-T800-coated sample, the Co coated sample, and the Zr substrate. The microhardness variation between the coating and the substrate is depicted in Fig.12 The Zr substrate exhibited a hardness of approximately 198 $HV_{0.2}$, the Co-T800 coating displayed a hardness of approximately 600 $HV_{0.2}$, and the pure Co coating exhibited a hardness of approximately 400 $HV_{0.2}$.

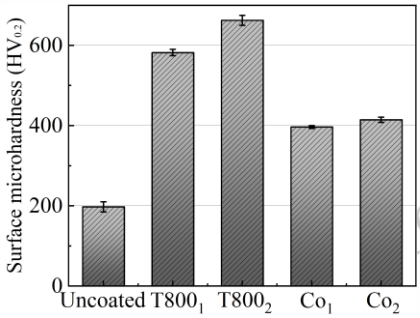

Fig.12 The microhardness variation between the coating and the substrate

Fig.13 displays the experimental findings on the surface morphology and friction coefficient of Co-based coatings and substrates after frictional wear. The detailed morphology of the wear contact surfaces of various coatings is depicted in Fig.13 (a-e). The uncoated sample has the greatest width of wear, accompanied by adhesive pits along the wear edge. This wear demonstrates the characteristics of adhesive wear and is characterized by its severity. In contrast, it was observed that all other

coating samples based on Co exhibited smoother wear edges and smaller widths of wear marks. The Co coating exhibited the narrowest abrasion mark width, with the Co-T800 coating ranking second in width. The variance in the maximum depth of the abrasion marks for the different samples is depicted in Fig.13 (f). A profilometer was used to measure the depth of the abrasion marks. The Co_1 and Co_2 coatings exhibit the least amount of abrasion marks, measuring around 1/4 of the substrate's depth. The Co-T800 coating is the second thinnest, with the abrasion marks reaching a maximum depth that is roughly half of the substrate's depth. On the Co-T800 coating, the maximum depth of abrasion marks is nearly half of the substrate, making it the second smallest coating.

Fig.13 (g) displays the abrasion trace obtained from the profilometer. The profile traces reveal that the uncoated samples exhibit a significantly larger abrasion profile compared to the Co-based coated specimens, both in terms of width and depth. Conversely, the abrasion traces of the Co_1 and Co_2 coated samples are comparatively smaller, with a slight disparity between the two. The Co-T800 coatings demonstrate a level of abrasion that falls within the range between that of the Co coatings and the substrate. The alteration in laser process parameters had a minimal impact on the shape of the coating's abrasion marks, both before and during the process modification. The coefficient of friction (COF) as a function of sliding time is depicted in Fig.13 (h).

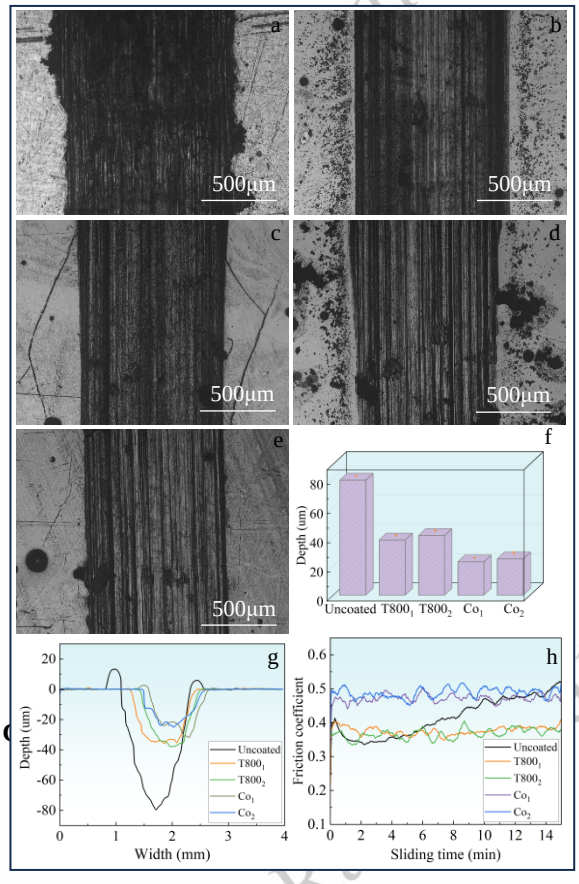

Fig.13 Abrasion mark morphology on the sample surface: (a) Zr substrate (b) $T800_1$ coating (c) $T800_2$ coating (d) Co_1 coating (e) Co_2 coating (f) abrasion depth (g) abrasion trajectory (h) friction factor

Through a comparative analysis of the coefficient of friction, it is observed that the substrate's coefficient of friction exhibits a gradual increase as the friction time increases. Additionally, the coated samples demonstrate a relatively stable coefficient of friction, potentially attributed to the specific nature of the friction between the substrate specimen and the friction vice. The experimental findings indicate that the application of laser melting Co and Co-T800 coatings enhances the wear resistance of the substrate, with the Co coating exhibiting the highest level of wear resistance. The alteration in the laser process has a minimal impact on the wear resistance of the coatings, resulting in a comparable level of wear resistance.

3 Conclusions

1) The compatibility of co-based coatings with both the substrate and the bonding characteristics between the coating and the substrate are favorable. By reducing the scanning rate and increasing the laser power, the coating thickness increased, leading to a slight improvement in coating quality. However, this alteration in the laser process parameters had a minimal impact on coating properties and did not enhance or deteriorate them.

2) The oxidized weight growth of the Co-based coated samples was significantly reduced compared to the substrate. The thickness of the oxygen diffusion layer in the coated samples was about 1/20-3/20 of that in the uncoated samples.

3) Zr has the highest corrosion resistance, followed by Co-T800 and Co coatings.

4) The hardness of the Co-T800 alloy coatings exceeded that of the pure metal Co coatings and the Zr substrate. the Co_1 and Co_2 coatings showed the smallest depth of wear marks, about 1/4 of the substrate. the Co-T800 coatings were the next thickest, with the maximum depth of the wear marks being about half the thickness of the substrate.

Chaoqun Xia, Bo Yang and **Hua Zhong**: Conceptualization, Methodology, Investigation, Writing - original draft preparation. **Bo Zhang**: Validation. **Shuguang Liu**, and **Qiang Li**: Data curation, Project administration, Writing - review & editing.

Declaration of Competing Interest

The authors declare that they have no known competing financial interests or personal relationships that could have appeared to influence the work reported in this paper.

Acknowledgments

This work was supported by the National Natural Science Foundation of China (Grant no. 52071126), the Natural Science Foundation of Tianjin City China (Grant No. 22JCQNJC01240), the Central Guidance on Local Science and Technology Development Fund of Hebei Province (226Z1009G), the Special funds for science and technology innovation in Hebei (2022X19) and the Anhui Provincial Natural Science Foundation (Grant No. 2308085ME135).

References

1 Wang Z, Yang X, Wang J, et al. *Crystals*[J], 2021,11(11): 1437.
2 Slobodyan, Mikhail. *Nuclear Engineering and Technology*[J], 2021,53(4): 1049-1078.
3 Ka-Yu H, Chuen-Horng T. *Journal of Nuclear Materials*[J], 1985,136(1): 16-29.
4 Zhou L J, Wang F, Yang C, et al. *Materials & Design*[J], 2015,78: 25-32.
5 Kondo R, Nomura N, Suyalatu, et al. *Acta Biomaterialia*[J], 2011,7(12): 4278-4284.
6 T K Sawarn, S Banerjee, A Samanta, et al. *Journal of Nuclear Materials*[J], 2015,467: 820-831.
7 Casucci A, Mazzitelli C, Monticelli F, et al. *Dental materials*[J], 2010, 26(8): 751-760.
8 Harooni A, Nasiri A M, Gerlich A P, et al. Journal of Materials Processing Technology[J], 2016,230: 263-271.
9 Chen Q S, Liu C H, Zhang R Q, et al. *Corrosion Science*[J], 2020,165: 108378.
10 Han X C, Chen C, Tan Y Q, et al. *Corrosion Science*[J], 2020,174: 108826.
11 Han X C, Xue J X, Peng S M, et al. *Corrosion Science*[J], 2019,156: 117-124.
12 Kashkarov E B, Sidelev D V, Syrtanov M S, et al. *Corrosion Science*[J], 2020,175: 108883.
13 Yeom H, Maier B, Johnson G, et al. *Journal of Nuclear Materials*[J], 2019,526: 151737.
14 Cheng Y L, Wu F, Dong J L, et al. *Electrochim Acta*[J], 2012,85: 25-32.
15 Malinovschi V, Marin A, Negrea D, et al. *Applied Surface Science*[J], 2018,451: 169-179.
16 Wang L, Luo Q, Zhang X, et al. *Bioactive materials*[J], 2020, 5(2): 377-386.
17 Mozetič M, Vesel A, Primc G, et al. *Thin Solid Films*[J], 2018, 660: 120-160.
18 Casucci A, Osorio E, Osorio R, et al. *Journal of dentistry*[J], 2009,37(11): 891-897.
19 Livingstone S, Xiao L, Corcoran E C, et al. *Nuclear Engineering and Design*[J], 2015,284: 97-105.
20 Shang X, Bo S, Guo Y, et al. *Applied Surface Science*[J], 2021,564: 150466.
21 Liu Y, Ding Y, Yang L, et al. *Journal of Manufacturing Processes*[J], 2021,66: 341-363.
22 Kim H G, Kim I H, Jung Y I, et al. *Journal of Nuclear Materials*[J], 2015,465:531-539.
23 Ocel ḱ V, De Oliveira U, De Boer M, et al. *Surface and Coatings Technology*[J], 2007,201(12): 5875-5883.
24 Houdkov S, Pala Z, Smazalová E, et al. *Surface and Coatings Technology*[J], 2017,318: 129-141.
25 Tong W, Sun B, Xu Q, et al. *IOS Press*[M], 2023: 172-177.
26 Shahroozi A, Afsari A, Khakan B. *Surface and Coatings Technology*[J], 2018,350: 648-658.
27 Weng F, Yu H J, Chen CH ZH, et al. *Journal of Alloys and Compounds*[J], 2016,686: 74-81.
28 Weng F, Yu H J, Liu J L, et al. *Optics & Laser Technology*[J], 2017,92: 156-162.
29 Xia C, Song L, Liu S, et al. *Materials Characterization*[J], 2021,174: 111045.
30 Fu Q, Zhu X, Li R, et al. *Energy Storage Materials*[J], 2020,30: 401-411.
31 Manhabosco T M, Tamborim S M, Dos Santos C B, et al. *Corrosion Science*[J], 2011,53(5): 1786-1793.
32 Li Q, Chen K, Xia C, et al. *Materials Science and Engineering: A*[J], 2021,817: 141358.
33 Maurya R, Siddiqui A R, Balani K. *Surface and Coatings Technology*[J], 2017,325: 65-74.
34 Xia C, Liu Q, Song T, et al. [J]. *Surface and Coatings Technology*, 2022,446: 128756.
35 Fu Y, Huang C, Du C, et al. [J]. *Corrosion Science*, 2021,191: 109727.
36 Yong Y W, Fu W, Deng Q L, et al. *Rare Metals*[J], 2017, 36: 934-941.

纯 Zr 表面激光熔覆 Co 基涂层高温氧化及耐蚀耐磨性能研究

夏超群[1]，杨博[1]，刘曙光[2]，张博[3]，钟华[4]，李强[1]

(1. 河北工业大学 材料科学与工程学院 天津市材料层状复合与界面控制技术重点实验室，天津 300130)

(2. 中国机械科学研究总院集团有限公司 北京机械工业自动化研究所有限公司，北京 100120)

(3. 天津大学 理学院化学系 天津市分子光电科学重点实验室，天津 300072)

(4. 合肥大学 先进制造工程学院，安徽 合肥 230000)

摘　要：本文采用激光熔覆技术制备 Co 基合金涂层锆合金，研究纯金属 Co 涂层与 T800 合金涂层高温氧化行为的差异以及涂层的耐磨性，并探讨改变激光熔覆工艺对涂层的影响。研究了两种涂层 Zr 合金样品在 800~1200 ℃ 下的氧化增重和高温 1 小时的高温氧化行为。结果分析表明，Co 涂层和 T800 涂层具有更好的抗高温氧化性能。在 1000 ℃ 下氧化 1 小时后，未涂层样品的氧化层厚度为 241 μm，而 Co 基涂层样品的氧化层厚度仅为 11.8～35.5 μm。经过摩擦磨损测试表明，涂层试样的磨痕深度仅为基体的 1/2，Zr 基体的硬度和耐磨性得到了很大提高。Co 基涂层的缺点是在 3.5% 的 NaCl 溶液中耐腐蚀性能较差。

关键词：金属Zr; 激光熔覆; Co基涂层; 高温氧化性; 耐磨性

作者简介：夏超群，男，1990 年生，博士，教授，河北工业大学天津市材料层状复合与界面控制技术重点实验室，天津 300130，E-mail: chaoqunxia@hebut.edu.cn

Figure captions

Table captions